

Reinforced silver chloride as a model material for the study of dislocations in metal matrix composites

David C. Dunand and Andreas Mortensen

Department of Materials Science and Engineering, Massachusetts Institute of Technology, Cambridge, MA 02139 (U.S.A.)

Abstract

Silver chloride containing fibers, spheres and particles of irregular form is used as a model material to study plasticity in metal matrix composites. Matrix dislocations generated upon cooling by the mismatch of coefficient of thermal expansion between the matrix and the reinforcement are observed by transmission optical microscopy after decoration at room temperature by photodissociation of the matrix. The plastic zone around the fibers, spheres and particles takes two forms: (a) trains of coaxial prismatic dislocation loops punched into the matrix and (b) a plastic zone of irregular form containing partially resolved tangled dislocations. A relationship between the inclusion volume and the volume of the plastic zone around a spherical or cylindrical inclusion in a strain-hardening matrix is presented and compared with experimental data. This relationship is extended to particles of irregular form.

1. Introduction

Elastic stresses are produced upon temperature change when the coefficients of thermal expansion (CTEs) of the two phases forming a composite differ. In composites where both phases are brittle (such as ceramic matrix composites or certain polymer matrix composites), these stresses can lead to the failure of one of the phases or the interface. In the case of metal matrix composites (MMCs), thermal stresses can be relieved by dislocation nucleation and glide in the matrix. This phenomenon has practical importance since most MMC systems are fabricated at a high temperature from which they are cooled, and since many MMCs are candidates for applications that involve thermal cycling.

Plasticity due to thermal mismatch between matrix and reinforcement has been investigated experimentally in metals reinforced with particles, whiskers or fibers, using etch pits [1, 2], slip lines [3] as well as transmission electron microscopy (TEM) [4–10]. However, these techniques do not allow complete and accurate observation of the dislocations in metals containing reinforcements of large size because only material in the immediate vicinity of a free surface, which perturbs both the dislocations and the stress state around the reinforcing phase, is observable. TEM

allows a very high resolution and is thus ideal for the observation of dislocations around second phases of small dimensions such as precipitation hardened metals. In most MMCs, however, the typical size of the reinforcement and its associated plastic zone is much larger than the thin area, in terms both of thickness and of width of the electron-transparent region. This hinders the investigation of some typical dislocation structures found in MMCs, such as long dislocations along the sides of fibers, or entire rows of punched dislocations extending far from the reinforcement.

To circumvent these limitations, we use silver chloride (AgCl) as a transparent model matrix for MMCs. This transparent salt has been used by many investigators to simulate metal plasticity since it exhibits dislocation mechanisms which are in most cases similar to those found in metals [11], leading to typically metallic properties such as strain hardening, high ductility or recovery. AgCl deforms at ambient temperature along the glide direction $\langle 110 \rangle$; the primary and secondary glide planes are respectively $\{110\}$ and $\{001\}$, thus leading to pencil glide.

Upon exposure to actinic light at room temperature, dislocations can be decorated within bulk AgCl by photodissociation and preferential precipitation of metallic silver on dislocation lines.

These can then be imaged by high resolution transmission optical microscopy [12–23], provided that the dislocation density is sufficiently low. In practice, silver halides must be chemically sensitized, in order to reach the maximum decoration depth of about $30\ \mu\text{m}$. This allows the observation of decorated dislocations associated with reinforcements of large dimension typically found in MMCs.

This experimental technique was developed by Mitchell and coworkers [16–23] over 30 years ago and led to some of the very earliest experimental evidence of the existence of dislocations. A review of this pioneering work is given in ref. 24. Interest in this technique for imaging dislocations subsequently waned with development of the transmission electron microscope, which allows direct observation of dislocations in metals at high resolution. While decoration techniques for examination in the optical microscope do not allow one to image individual dislocations when their density is high, we believe that they present distinct advantages over alternative techniques mentioned above for the study of the plastic zone around supramicroscopic reinforcements typically used in MMCs, because the whole plastic zone can be examined. Furthermore, the equilibrium configurations of low density dislocation structures which extend far from the reinforcement, such as prismatic loop rows, can be examined in their entirety.

In what follows, we present a detailed account of sample preparation techniques. We then summarize research to date where we used AgCl to study dislocations produced by thermal mismatch of a reinforcing phase such as spheres, particles of irregular shape and fibers [25, 26] in a ductile matrix deforming by slip. Examples of dislocation structures are presented in the form of micrographs and a simple geometrical model predicting the volume of the plastic zone around reinforcements of different shapes in a strain-hardening matrix is compared with experimental data.

2. Experimental procedures

We closely follow the experimental methods developed by Mitchell and coworkers [16–24]. Great care must be exercised in each of the steps to obtain optimal microstructures. Blocks of AgCl (99.999% purity, purchased from Engelhard, OH) are cut with a razor blade, cleaned for 10 min in a 10% HCl solution, rinsed in distilled

water and dried at about 400 K in air. The cuttings are charged in a Pyrex crucible and melted under dry nitrogen by heating the glass apparatus shown in Fig. 1(a) with an oxygen-gas flame. The melt is purified by slowly bubbling 99.9% pure chlorine for about 15 min, to transform silver oxide or metallic silver into chloride. This operation is stopped when no oxide layer is visible at the top of the melt. The melt is then degassed for about 15 min by bubbling dry nitrogen, solidified and cooled to room temperature under the same atmosphere. The ingot is then transferred to a capillary filter (Fig. 1(b)), heated in dry nitrogen until a drop of liquid runs down the capillary and seals it by solidifying at its tip and is then completely melted. The melt is then run through the capillary into a cold crucible by melting the small drop of chloride blocking the capillary tip. Any

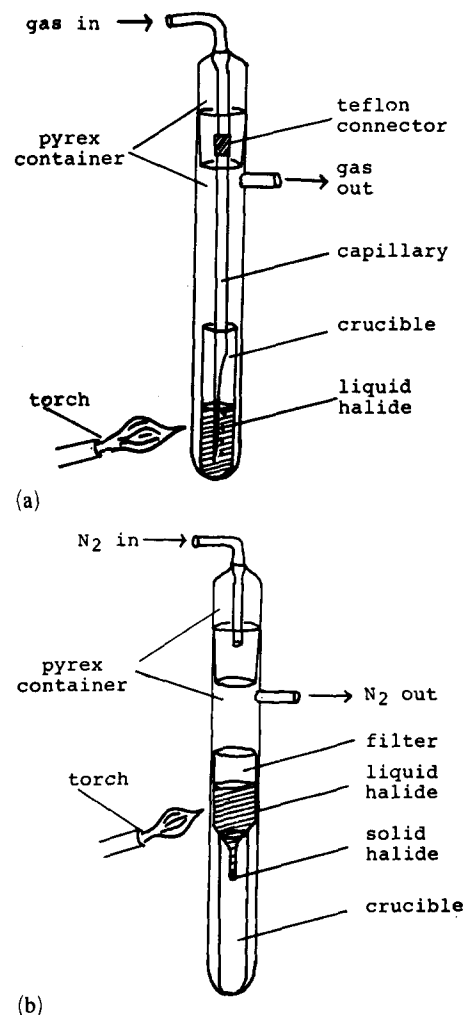


Fig. 1. (a) Apparatus used to purify the AgCl melt. (b) Apparatus used to filter the AgCl melt.

solid particles, silver oxide or colloidal silver present in the melt are deposited on the walls of the filter. This filtering operation is repeated until no residues are left on the walls of the filter. The AgCl is then doped with 500 wt.ppm cuprous chloride (99.999% purity powder purchased from Strem Chemicals, MA), by melting both compounds in a crucible under dry nitrogen and thoroughly mixing them in the liquid state by shaking the apparatus. The previous degassing operation is crucial for the success of this last step since any free chlorine will transform the cuprous chloride into cupric chloride, with a subsequent loss of sensitization. All operations involving the reactive molten AgCl are performed in Pyrex or quartz glassware, previously aged in boiling nitric acid for 15 min and thoroughly rinsed in distilled water prior to each experiment to avoid contamination by leached metallic ions.

The reinforcements used are glass microspheres (borosilicate Corning glass 7070) with a diameter range of 1–5 μm , glass particles (borosilicate glass BK10) in the same dimension range, and glass continuous fibers (strontium oxide glass) with a diameter range from 0.8 to 2 μm , all purchased from MoSci Corporation (Rolla, MO). Chopped SafimaxTM alumina (Al_2O_3) fibers 3 μm in diameter are also used (Imperial Chemical Industries, Runcorn, U.K.). A slurry of the reinforcement in pure acetone is spread on two quartz plates, which are then covered with a clean glass funnel to avoid dust contamination, and preheated to about 823 K. Doped AgCl is melted under flowing dry nitrogen in a capillary and poured onto one of the hot quartz plates, on which two quartz spacers 100 μm thick have previously been placed. The melt is then topped as quickly as possible by the other hot quartz plate and pushed at a speed of about 10 $\mu\text{m s}^{-1}$ onto a water-cooled chill, thus directionally solidifying the composite silver halide plate (Fig. 2). In every instance, millimeter-sized bubbles—probably due to shrinkage—formed at the solid–liquid front. These could not be eliminated even when the sample was solidified vertically and/or submitted to vibrations. Since their volume fraction is small, they do not disturb observation of the microstructure.

The cast composite is then separated from the quartz plates in distilled water and cut into smaller samples with a razor blade. The samples are subsequently annealed to remove the dislocations introduced by the differential contraction of

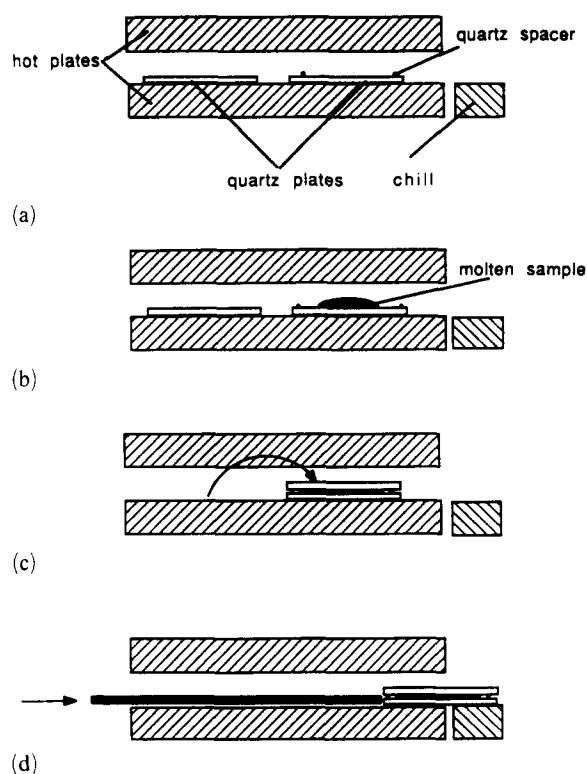


Fig. 2. Schematic diagrams of sample fabrication: (a) oven configuration; (b) melt transfer; (c) plate fabrication; (d) sample solidification.

the quartz plates and the specimen. The sample is annealed in a tube furnace on a quartz plate under flowing dry nitrogen for 2 h at 673 K and gas cooled to room temperature at a rate of about 1 K s^{-1} . Each sample is finally exposed for a few hours to the unfiltered light of a stroboscope (model 510AL, Electronic Brazing Company) with the following characteristics: xenon tube, 60 flashes s^{-1} , integrated illuminance per flash of 35 lux s^{-1} . Immediately thereafter, the samples are mounted on a microscope slide and the decorated substructure is observed in transmitted light and recorded photographically using a Zeiss metallurgical microscope with a 100 \times oil immersion lens.

3. Results

All heat-treated samples show small black surface precipitates (1–5 μm in radius) which are not present in the as-cast condition. These precipitates, which are limited to the surface, do not form in non-sensitized control samples and must be related to the presence of the cuprous ions; however, they do not seem to interfere with

the microstructure in the bulk. In all samples, submicron random precipitation of silver takes place within the AgCl upon exposure to actinic light, resulting in the "fog" visible in all micrographs. Unproperly sensitized samples display heavy surface fog at the surface which hides the decorated substructure. The high intensity stroboscopic light yields better and deeper decoration than continuous exposure to the light of a mercury vapor lamp with or without an outer glass envelope. The first features to be decorated are always grain and subgrain boundaries; only when the samples are properly sensitized can individual dislocations be decorated. The resolution depends on both the dislocation density and the amount of silver precipitated on the dislocation line. In most samples, decoration is found to fade in a matter of hours when the samples are exposed to the light of the microscope, or days when exposed to daylight. Subsequent exposure to actinic light increases the background fog rather than restores the decoration.

Misfitting inclusions punch dislocation loops along crystallographic directions as observed by Mitchell [21] for glass spheres and by Parasnis and Mitchell [23] for silver precipitates. Figure 3 shows an example of submicroscopic precipitates (probably silver specks) which punched rows of loops along the six $\langle 110 \rangle$ directions in the $\{111\}$

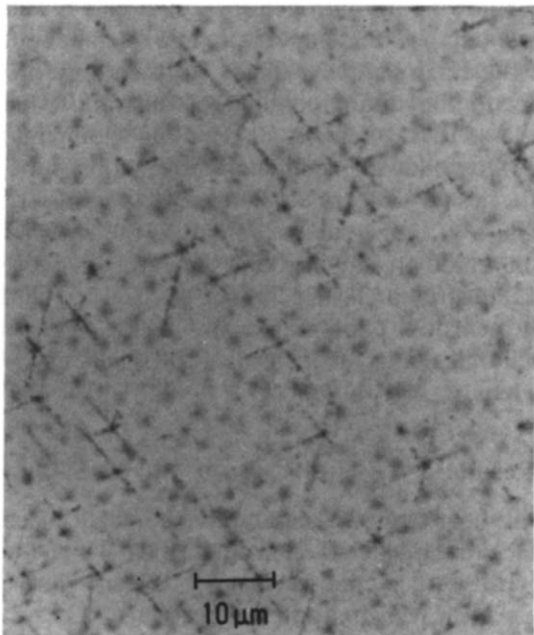


Fig. 3. Decorated submicroscopic loops punched along $\langle 110 \rangle$ directions by small particles. The micrograph plane is parallel to $\{111\}$.

plane which is parallel to the image plane. Much larger glass spheres exhibit the same relaxation mechanism but along only one or two directions (Figs. 4 and 8), and two adjacent glide cylinders are rarely observed to be activated simultaneously. This can be explained by the fact that adjacent glide cylinders overlap close to the sphere if the model described by Hull and Bacon [27] is considered, wherein dislocations are nucleated at the locus of maximal shear stress on the sphere surface (Fig. 5). The overlapping volume, shaded in Fig. 5, increases with increasing volume of the sphere, as does the probability that two punched loops interact with each other and form a stable sessile product [28]. Once such a lock is produced, the subsequent punched dislocations are not able to glide away from the interface but instead further interact and form a

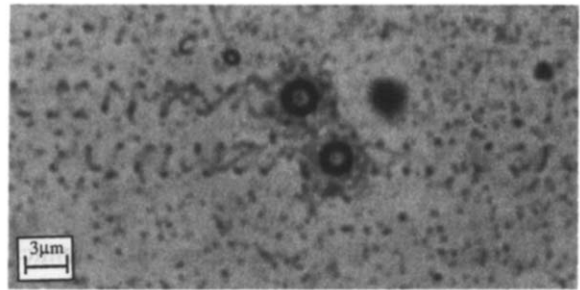


Fig. 4. Rows of decorated prismatic loops punched by two glass spheres. Some loops form figures of eight and more complicated figures. Unresolved tangles are also visible around the spheres.

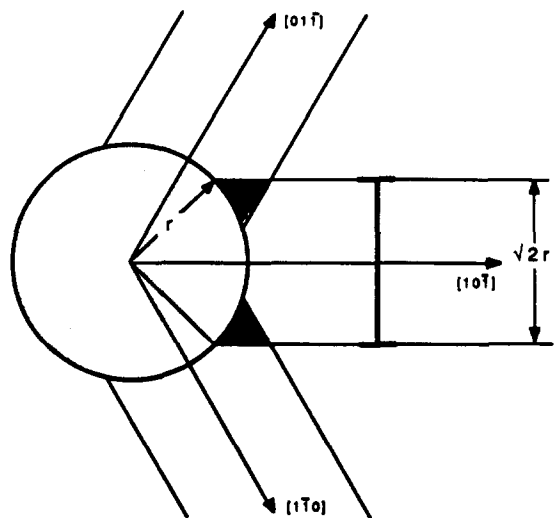


Fig. 5. Schematic diagram of prismatic dislocation loops punched in the $\langle 110 \rangle$ directions of an f.c.c. lattice from a sphere [27]. The shaded volumes represent the intersection of adjacent glide systems.

dense region of tangled dislocations as observed in metals containing submicroscopic inclusions by TEM [29–31]. Such plastic regions of high dislocation densities are visible in decorated silver halide as a black region surrounding the spheres (Figs. 6 and 7) in which individual dislocations can sometimes be resolved. The coexistence of a train of loops and a plastic zone of tangled dislocations can be explained as resulting from relaxation first taking place by punching along one direction, followed by entanglement when adjacent overlapping glide cylinders become active.

The plastic zone morphology around particles of irregular form is qualitatively very similar to that around spheres; relaxation takes place by punching along a crystallographic direction and leads to a tangled zone of high dislocation density

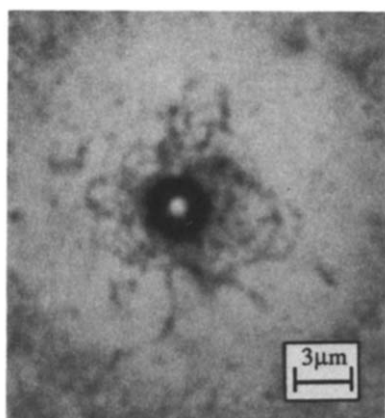


Fig. 6. Partially resolved tangled decorated dislocations forming a plastic zone around a glass sphere.

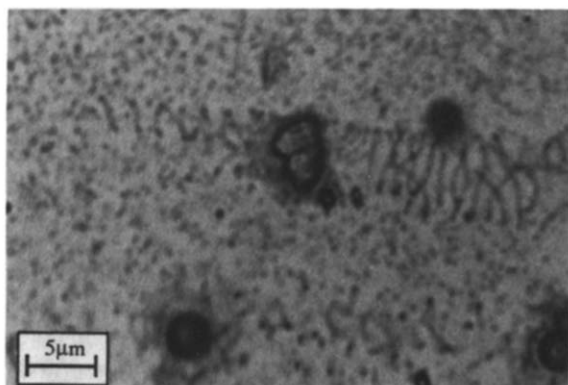


Fig. 7. Glass particle of irregular form having punched two rows of decorated prismatic loops. The particle is also surrounded by a zone of dense unresolved decorated dislocations, as is the glass sphere at the bottom left of the micrograph.

when other glide cylinders are activated (Fig. 7). In other instances, only the zone of tangled dislocations is observed (Fig. 8), which suggests that in such cases punching initiated simultaneously in many directions, leading to immediate entanglement. A difference from the spherical case is that particles have sharp corners, where stress concentration of which is often found to nucleate dislocation punching (Fig. 9). Also, for non-equiaxed particles, punching is found to initiate predominantly in the direction of the particle's largest dimension. This reflects the fact that mismatch is maximal in that direction and therefore punching is activated earlier.

Figure 10 presents examples of particle and plastic zone projected shapes as seen in the microscope. The plastic zone does not form a shell of constant thickness around the particle, possibly because relaxation starts earlier at one place, or because entanglement does not occur at the same distance from the interface. It can be concluded from this observation that large errors might be introduced if TEM measurements (such as dislocation density or plastic zone extent) are made only at one limited region of the interface and are generalized to the whole plastic zone.

Fibers share with elongated particles the feature of a main direction along which mismatch is maximal; the fiber tip also acts as a stress concentrator owing to its sharp corner. As a consequence, punched loops are generated there to relax the fiber axial mismatch stress (Fig. 11). When the fiber axis does not correspond to a glide direction, punching nevertheless takes

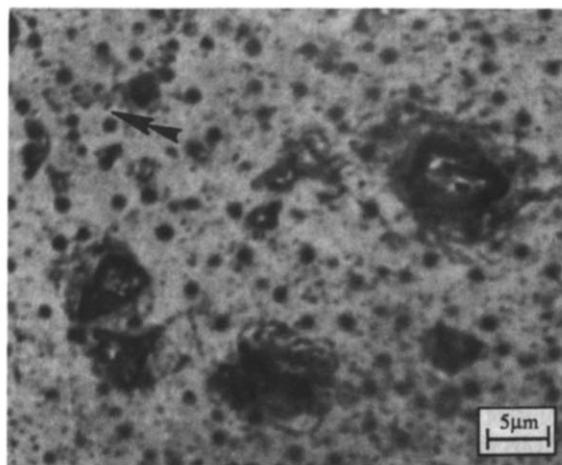


Fig. 8. Partially resolved tangled decorated dislocations around glass particles forming a dense plastic zone. A small particle has punched four decorated loops (arrow).

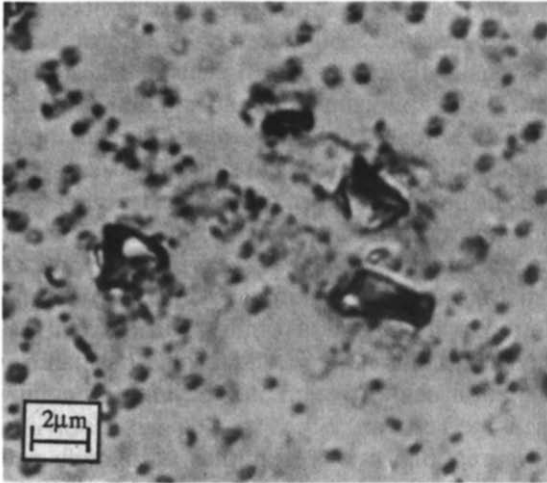


Fig. 9. Row of punched decorated loops emitted by the corners of an elongated glass particle.

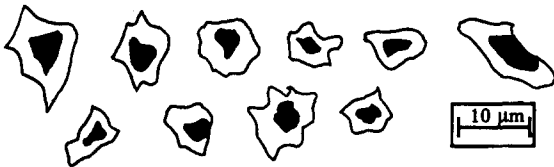


Fig. 10. Outlines of particles and their associated plastic zones traced by hand from enlarged micrographs. There is no correlation between the shape of a particle and that of its plastic zone.

place, albeit at an angle (Fig. 12). Many dislocation geometries are possible to relax the radial stresses. If the simple model of punching is adopted for the radial mismatch, long loops are assumed to nucleate at the fiber–matrix interface from which they glide away owing to the elastic mismatch stress (Fig. 13). Because of their large size, these loops are likely to be blocked rather early in their motion by other obstacles in the matrix, such as small precipitates or statistical dislocations. Also, the intersection volume between adjacent glide systems is very large (shaded area in Fig. 13). We therefore rarely observe rows of long dislocations punched along the sides of a fiber as in Fig. 14, since long dislocations have a high probability of getting blocked, at which point they form an obstacle to subsequent loops produced at the interface. This induces entanglement and results in a plastic zone of dense dislocations, which is very often observed around fibers as a dark cylindrical zone in which decorated dislocations can sometimes be resolved (Fig. 15(a)). The edge of the plastic zone is sometimes made of subgrain boundaries

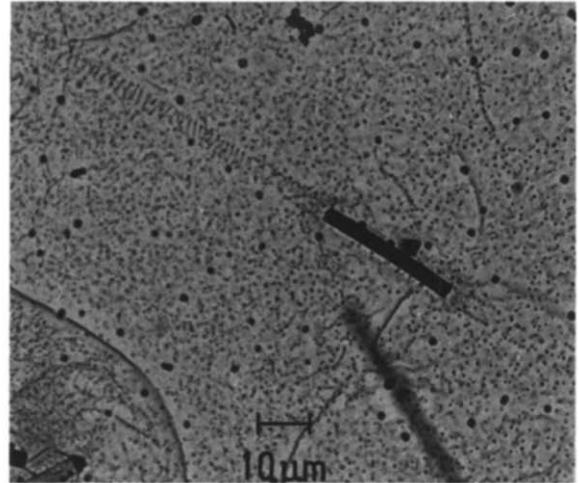


Fig. 11. Decorated rows of prismatic loops punched by a short Al_2O_3 fiber. The linear feature at the bottom left of the micrograph is a decorated subgrain boundary.

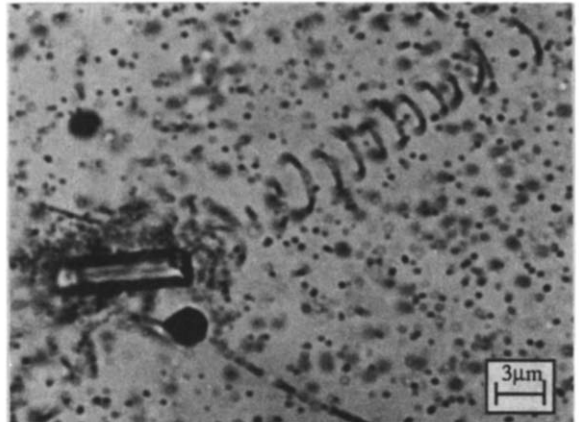


Fig. 12. Short Al_2O_3 fiber which punched a row of decorated loops, the axis of which forms an angle with that of the fiber. The fiber is also surrounded by a decorated plastic zone of unresolved dislocations.

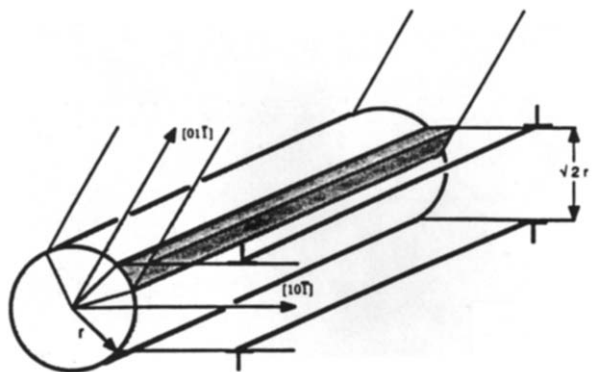


Fig. 13. Schematic diagram of prismatic dislocation loops, punched in the $\langle 110 \rangle$ directions of an f.c.c. lattice from a cylinder. The shaded volumes represent the intersection of adjacent glide systems [25].

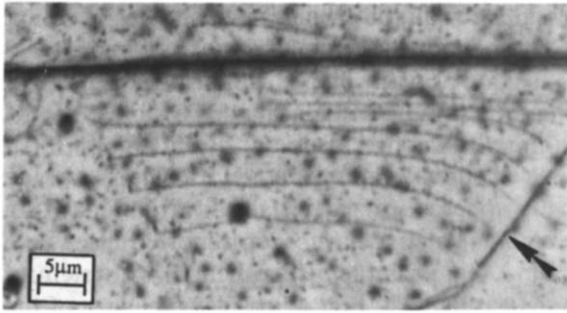


Fig. 14. Decorated linear dislocations emitted by the sides of a glass fiber. A decorated subgrain boundary is marked by an arrow.

(Fig. 15(b)), thus leading to the conclusion that dislocation rearrangement takes place in the plastic zone.

4. Modeling

In work reported elsewhere [25], we propose a simple model to calculate the size of the plastic zone surrounding spheres and cylinders, which takes account of the influence of dislocation density on matrix flow stress. We assume that dislocations are punched according to Figs. 5 and 13 and distribute them uniformly within the plastic zone, which we assume to have a uniform flow stress given by the classical work-hardening relationship linking the yield stress in shear τ_y of the matrix to the local dislocation density ρ :

$$\tau_y = \tau_{y0} + AGb\rho^{1/2} \quad (1)$$

where τ_{y0} is the matrix yield stress in shear before strain hardening, G is the matrix shear modulus, b is the dislocation's Burgers vector and A is the strain-hardening constant (A is zero for a non-strain-hardening material; $A=0.3-0.6$ for most metals and 0.4 for NaCl).

We use a solution by Hill [32] which gives the plastic zone radius due to the expansion of a spherical or cylindrical cavity into an infinite isotropic linear elastic non-work-hardening plastic matrix to predict the volume of the plastic zone and the associated dislocation density around a cylindrical and spherical inclusion. This yields a linear relationship between the radius r of the inclusion and the radius c of the plastic zone in a non-work-hardening matrix. The solution for the sphere is identical with that developed by Kim *et al.* [10] using a different approach. We then introduce eqn. (1) to derive simple equations predicting the size of the plastic zone around a

cylindrical or spherical inclusion in a strain-hardening matrix:

$$x^3 - x^2(1 + C_1 + 2C_2) + x(C_2^2 + 2C_2) - C_2^2 = 0 \quad (2)$$

where, for a cylindrical inclusion and its plastic zone of respective radii r_c and c_c

$$x = \left(\frac{c_c}{r_c}\right)^2$$

$$C_1 = \frac{2^{3/2} \Delta\alpha \Delta T b}{r_c} \left(\frac{AG}{\tau_{y0}}\right)^2 \quad (3a)$$

$$C_2 = \frac{\Delta\alpha \Delta T G(1 + \nu)}{\tau_{y0}(1 - \nu)}$$

and, for a spherical inclusion of radius r_s and the associated plastic zone of radius c_s

$$x = \left(\frac{c_s}{r_s}\right)^3$$

$$C_1 = \frac{6 \times 2^{1/2} \Delta\alpha \Delta T b}{r_s} \left(\frac{AG}{\tau_{y0}}\right)^2 \quad (3b)$$

$$C_2 = \frac{4 \Delta\alpha \Delta T G(1 + \nu)}{\tau_{y0}(5 - 4\nu)}$$

$\Delta\alpha$ is the CTE difference between the matrix and the inclusion, ν is the Poisson's ratio for the matrix and ΔT is the temperature excursion for which slip is operational.

Figure 16 shows the experimental data for AgCl reinforced with glass spheres. The non-strain-hardening equation predicts a plastic zone volume (including the sphere volume) about six times larger than eqns. (2) and (3b) which take into account strain hardening of the matrix and matches the data well. The plastic zone volume around Al_2O_3 fibers of radius $1.5 \mu\text{m}$ in AgCl (measured from the fiber axis) was found to be 63% higher than the prediction of eqns. (2) and (3a) while the non-strain-hardening model overestimates it by 191%.

In a subsequent publication [26], we extend the model developed for spheres to mismatching particles of irregular shape, which are more typical of particle-reinforced MMCs, by making the assumption that a sphere and a particle of the same volume generate a plastic zone of identical volume. This assumption is based on the fact that the thermal mismatch that must be relieved by

dislocation punching is proportional to the volume of the inclusion and the average length of the dislocations is about the same in the spherical and particular cases. This last point is supported by the experimental observation of rows of loops

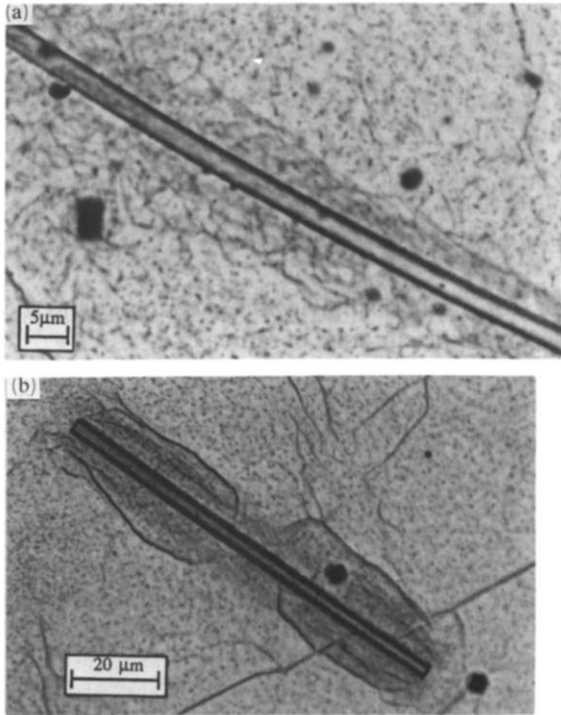


Fig. 15. (a) Partially resolved tangled decorated dislocations part of the plastic zone around a long Al_2O_3 fiber. (b) Un-resolved decorated dislocations around an Al_2O_3 fiber. The linear features separating the plastic zone from the non-decorated matrix are subgrain boundaries.

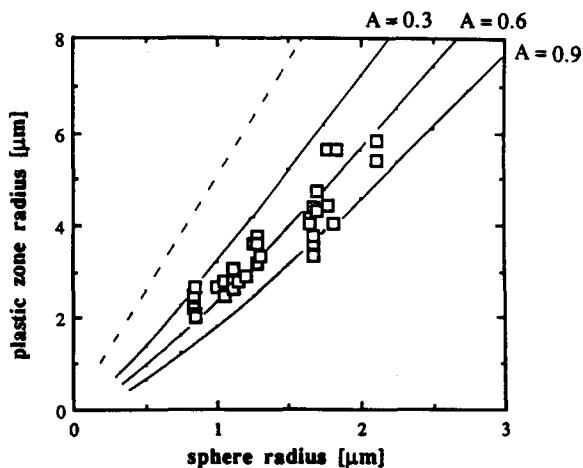


Fig. 16. Radius of plastic zone surrounding spheres in an AgCl matrix as a function of the radius of the corresponding spheres [25]: \square , experimental data; —, strain-hardening matrix with different values of A (eqn. (2)); ---, non-strain-hardening matrix. The constants for the material are listed in Table 1.

of similar radii for particles and spheres of equivalent volume. Agreement with experimental data is as good as with spheres, confirming the importance of strain hardening and the simple model summarized above.

Predictions from this model for silicon carbide (SiC) spheres (or particles) and cylinders in an aluminum matrix have been reported elsewhere [25]. As an example of another MMC system of practical interest, Fig. 17 displays the size of the plastic zone around SiC cylinders in a titanium matrix for a ΔT value of 800 K, using a CTE value for SiC of $3.4 \times 10^{-6} \text{ K}^{-1}$ and the constants given in Table 1. The plastic zone radius that results from the use of eqns. (2) and (3b) with $A=0$ for a non-strain-hardening matrix is also

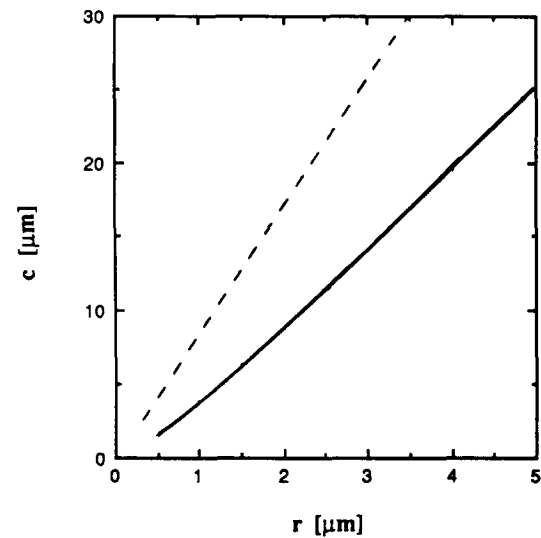


Fig. 17. Plastic zone radius around an SiC fiber in a titanium matrix after a temperature change of 800 K: —, strain-hardening matrix (eqn. (2)); ---, non-strain-hardening matrix. The constants for the material are listed in Table 1.

TABLE 1

Thermomechanical parameters of matrix materials (high purity AgCl and unalloyed titanium)

Parameter (units)	Ti	AgCl
α (K^{-1})	8.41×10^{-6}	3×10^{-5}
E (GPa)	120	26
G (GPa)	46	6.9
ν (-)	0.36	0.343
b (nm)	0.295 ^a	0.384
τ_{y0} (MPa)	13.7 ^a	0.5
A (-)	0.5	0.6

^aTitanium with 0.01 wt.% O and N with a {1100} slip plane [33].

given in the same figure. The non-strain-hardening model predicts a plastic zone volume (including the fiber volume) about three times larger than given by eqns. (2) and (3b). For a fiber $10\ \mu\text{m}$ in diameter, the dislocation density in the plastic zone is $3.2 \times 10^{11}\ \text{m}^{-2}$ and the increase in yield stress in shear in the plastic zone due to the dislocations is 3.8 MPa and is thus more than a quarter of the intrinsic flow stress of 13.7 MPa reported by Honeycombe [33]. The volume fraction of reinforcement at which the plastic zones calculated by eqns. (2) and (3b) start to touch in an ideal hexagonal packing is 3.6%. Since the model was developed for a single inclusion in an infinite matrix, it is not valid at or above this volume fraction. The dislocation density and yield stress increase calculated above are thus likely to be lower bound values when the plastic zones of adjacent fibers interact.

5. Conclusions

(1) Quenched AgCl, containing fibers, microsphere and irregularly shaped particles, is used as a model material to study thermally induced plasticity in MMCs. Dislocations decorated at room temperature by photodissociation of the matrix are observed by transmission optical microscopy in thick samples. While this technique has a low resolution, it allows the observation of a large volume of undisturbed material and is thus complementary to TEM for investigating the plastic zone around supramicroscopic inclusions.

(2) Thermal mismatch stresses around fibers, spheres and particles generate dislocations that take the form of rows of prismatic loops extending far away from the interface and/or tangles forming a well-defined plastic zone surrounding the inclusion. This leads to the hypothesis that the zone of dense dislocations was formed from prismatic dislocations which got entangled before they could glide away from the interface. Nucleation of prismatic loops is observed at sharp corners at particles and fiber ends, probably stimulated by the local stress concentration.

(3) A model is presented that predicts the volume of the plastic zone due to thermal mismatch of a low volume fraction of spherical and cylindrical inclusions in a strain-hardening matrix; it is found to fit the data for AgCl well. While there is no correlation between the shape of an irregular particle and that of its plastic zone, its volume can be predicted by adapting the

model for a sphere. The plastic zone volume around irregular glass particles in AgCl is found to match the predictions of the model well. Particles of irregular form can thus be assimilated to spheres, therefore significantly simplifying modelling of the plastic zone volume in particle-reinforced metals.

Acknowledgments

This work was supported by the Office of Naval Research under Contract N00014-89-J-1541, monitored by Dr. S. G. Fishman. We also wish to express our most grateful appreciation to Professor J. W. Mitchell at the University of Virginia for advice in the initial stages of our experimental research.

References

- 1 K. K. Chawla and M. Metzger, *J. Mater. Sci.*, 7 (1972) 34.
- 2 K. K. Chawla and M. Metzger, *Metall. Trans. A*, 8 (1977) 1680.
- 3 Y. Flom and R. J. Arsenault, *Mater. Sci. Eng.*, 75 (1985) 151.
- 4 R. J. Arsenault and R. M. Fisher, *Scr. Metall.*, 17 (1983) 67.
- 5 S. P. Rawal, L. F. Allard and M. S. Misra, in A. K. Dhingra and S. G. Fishman (eds.), *Interfaces in Metal Matrix Composites*, AIME, New York, 1986, p. 211.
- 6 S. P. Rawal, L. F. Allard and M. S. Misra, in F. L. Matthews, N. C. R. Buskell and J. M. Hodginson (eds.), *Proc. 6th Int. Conf. on Composite Materials*, Elsevier Applied Science, London, 1987, p. 2.16.
- 7 M. Vogelsang, R. J. Arsenault and R. M. Fisher, *Metall. Trans. A*, 17 (1986) 379.
- 8 M. Taya and T. Mori, *Acta Metall.*, 35 (1987) 155.
- 9 Q. Li, J. Megusar, L. J. Masur and J. A. Cornie, *Mater. Sci. Eng.*, A117 (1989) 199.
- 10 C. T. Kim, J. K. Lee and M. R. Plichta, *Metall. Trans. A*, 21 (1990) 673.
- 11 M. T. Sprackling, *The Plastic Deformation of Simple Ionic Crystals*, Academic Press, New York, 1976.
- 12 H. Layer, M. G. Miller and L. M. Slifkin, *J. Appl. Phys.*, 33 (1962) 478.
- 13 L. M. Childs and C. B. Slifkin, *Br. J. Appl. Phys.*, 16 (1965) 771.
- 14 J. R. Haynes and W. Shockley, *Phys. Rev.*, 82 (1951) 935.
- 15 P. Süptitz, *Z. Phys.*, 153 (1958) 174.
- 16 J. M. Hedges and J. W. Mitchell, *Philos. Mag.*, 7 (1953) 223.
- 17 J. M. Hedges and J. W. Mitchell, *Philos. Mag.*, 7 (1953) 357.
- 18 P. V. Clark and J. W. Mitchell, *J. Photogr. Sci.*, 4 (1956) 1.
- 19 J. W. Mitchell, *Dislocations and Mechanical Properties of Crystals*, Wiley, New York, 1957, p. 69.
- 20 D. A. Jones and J. W. Mitchell, *Philos. Mag.*, 3 (1958) 1.
- 21 J. W. Mitchell, *Growth and Perfection of Crystals*, Wiley, New York, 1958, p. 386.

- 22 J. W. Mitchell, *Faraday Discuss. Chem. Soc.*, 28 (1959) 242.
- 23 A. S. Parasnis and J. W. Mitchell, *Philos. Mag.*, 8 (1959) 171.
- 24 J. W. Mitchell, *Proc. R. Soc. London, Ser. A*, 371 (1980) 149.
- 25 D. C. Dunand and A. Mortensen, *Acta Metall. Mater.*, 39 (1991) 127.
- 26 D. C. Dunand and A. Mortensen, *Mater. Sci. Eng., A*, 135 (1991) 179.
- 27 D. Hull and D. J. Bacon, *Introduction to Dislocations*, 3rd edn., Pergamon, Oxford, 1984, p. 166.
- 28 W. C. Johnson and J. K. Lee, *Acta Metall.*, 31 (1983) 1033.
- 29 M. H. Lewis and J. M. Martin, *Acta Metall.*, 11 (1963) 1207.
- 30 M. F. Ashby, S. H. Gelles and L. E. Tanner, *Philos. Mag.*, 19 (1969) 757.
- 31 B. J. Makenas and H. K. Birnbaum, *Acta Metall.*, 28 (1980) 979.
- 32 R. Hill, *The Mathematical Theory of Plasticity*, Oxford University Press, Oxford, 1950.
- 33 R. W. K. Honeycombe, *The Plastic Deformation of Metals*, 2nd edn., American Society for Metals, Metals Park, OH, 1984, p. 115.